

# Rotational Pattern Difference in Resolved Fluorescence Spectra with Different Detection Schemes

Hongmin Chen,<sup>\*1</sup> Li Li,<sup>\*2</sup> G. Lazarov,<sup>†</sup> X. Wang,<sup>†</sup> A. M. Lyyra,<sup>†</sup> J. Huennekens,<sup>‡2</sup> and R. W. Field<sup>§3</sup>

<sup>\*</sup>Department of Physics, Tsinghua University, Beijing 100084, China; <sup>†</sup>Department of Physics, Temple University, Philadelphia, Pennsylvania 19122;

<sup>‡</sup>Department of Physics, Lehigh University, 16 Memorial Drive East, Bethlehem, Pennsylvania 18015; and

<sup>§</sup>Department of Chemistry, Massachusetts Institute of Technology, Cambridge, Massachusetts 02139

E-mail: [jph7@lehigh.edu](mailto:jph7@lehigh.edu)

Received June 1, 1998; in revised form March 31, 1999

The relative intensities of rotational lines in resolved fluorescence spectra are dependent on the detection direction and the choice of the detection scheme when a grating monochromator is used. These differences arise from the spatially anisotropic distribution of the fluorescence, the rotational branch dependence of the fluorescence polarization, and the polarization dependence of the monochromator grating efficiency. Both the anisotropy of the emission and the rotational branch dependence of the fluorescence polarization are enhanced in double-resonance excitation schemes. In the present work, we analyze the relative intensities in the  ${}^7\text{Li}_2$   $1^3\Sigma_g^- \rightarrow 1(b)^3\Pi_u$  and  $1^3\Delta_g \rightarrow 1(b)^3\Pi_u$  resolved fluorescence spectra, observed following double-resonance excitation, for three different detection schemes. © 1999 Academic Press

**Key Words:** fluorescence detection; spectral patterns of fluorescence;  ${}^7\text{Li}_2$ -resolved fluorescence; polarization of fluorescence.

## I. INTRODUCTION

Laser-induced fluorescence (LIF) has become a classic technique of laser spectroscopy. LIF spectra are recorded in two formats, *fluorescence excitation* and *resolved fluorescence*. A fluorescence excitation spectrum is recorded by monitoring total fluorescence while the laser frequency is scanned. Resolved fluorescence spectroscopy involves scanning the monochromator while holding the laser frequency fixed to a selected transition.

Resolved fluorescence spectra provide abundant information about the upper and lower states. Relative intensities of transitions into different vibrational levels of the lower state give information about Franck–Condon factors and transition dipole moments. The rotational structure of a transition (spectral patterns and relative intensities of rotational lines), from a single upper rovibronic level to a lower vibrational level, is often used to determine the symmetries of the upper and lower states.

In resolved fluorescence experiments, the laser-induced fluorescence can be collected with several different detection schemes. The relative intensities of rotational lines in the resolved fluorescence spectra, however, may depend on the particular scheme chosen. For experiments utilizing double-resonance excitation, the polarization behavior is much more

complex than the well-understood and frequently treated one photon excitation case. Here we show examples and quantitatively explain the differences in the relative rotational branch intensities for perturbation-facilitated optical–optical double-resonance (PFOODR) resolved fluorescence spectra of  ${}^7\text{Li}_2$ , as studied using three of the most common geometries.

## II. OBSERVATIONS

The experimental setup has been described in Refs. (1) and (2). Lithium vapor was generated in a *five-arm* heatpipe oven [Fig. 1a]. Two continuous-wave (CW) single-mode, frequency-stabilized CR 699-29 dye lasers were used as the PUMP and PROBE lasers to excite  $1^3\Sigma_g^- (v = 0, N = 9, J = 10) \leftarrow b^3\Pi_u (v' = 19, N' = 10, J' = 11) \leftarrow X^1\Sigma_g^+ (v'' = 4, J'' = 10)$ ,  $1^3\Delta_g (v = 9, N = 9, J = 10) \leftarrow b^3\Pi_u (v' = 19, N' = 10, J' = 11) \leftarrow X^1\Sigma_g^+ (v'' = 1, J'' = 10)$ , or  $1^3\Delta_g (v = 17, N = 9, J = 10) \leftarrow b^3\Pi_u (v' = 19, N' = 10, J' = 11) \leftarrow X^1\Sigma_g^+ (v'' = 1, J'' = 10)$  transitions of  ${}^7\text{Li}_2$ . The  $b^3\Pi_u (v' = 19, N' = 10, J' = 11)$  intermediate level is perturbed by the  $A^1\Sigma_u^+ (v' = 13, J' = 11)$  level and therefore acts as a *window* level through which the *dark* triplet states can be viewed. Both lasers were linearly polarized along the same direction and co- or counterpropagated coaxially. OODR fluorescence from the upper  $1^3\Sigma_g^-$  or  $1^3\Delta_g$  level excited by the lasers, to the  $b^3\Pi_u$  state, was resolved with a Spex 0.85 m double-grating monochromator. The relative detection system efficiency, as a function of wavelength, was measured using a calibrated tungsten–halogen lamp (“white light source”) (3).

<sup>1</sup> Present address: Department of Physics, University of Connecticut, U-46, Storrs, CT 06269.

<sup>2</sup> To whom correspondence should be addressed.

<sup>3</sup> Also at Department of Physics, Tsinghua University, Beijing 100084 China.

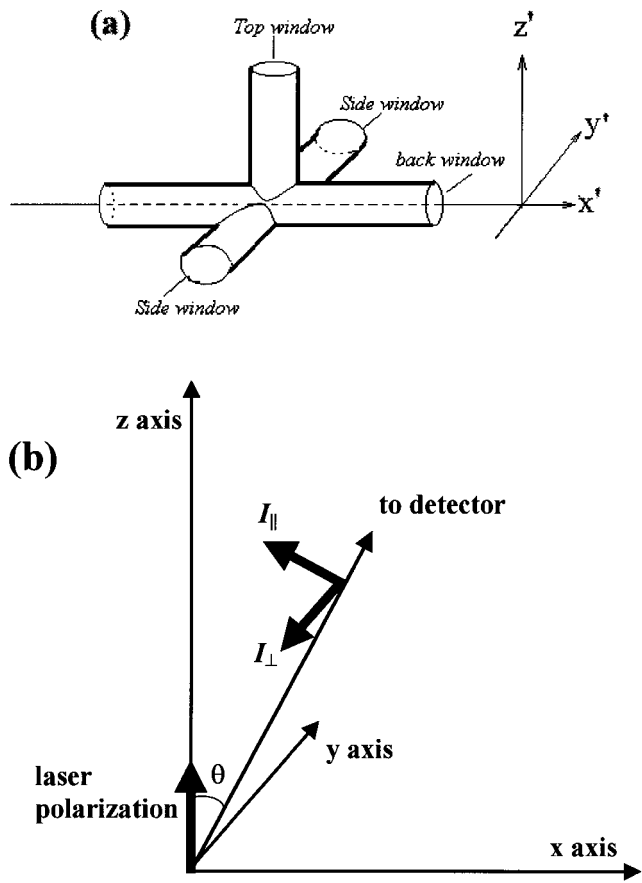


**FIG. 1.** (a) The heat pipe oven with the space fixed ( $x'$ ,  $y'$ ,  $z'$ ) coordinate axes. (b) The laser polarization and fluorescence collection ( $x$ ,  $y$ ,  $z$ ) coordinate axes and the two polarization components  $I_{\perp}$  and  $I_{\parallel}$  of the detected fluorescence perpendicular and parallel to the  $xz$  plane, respectively.

Since the reflection efficiency of the two monochromator gratings depends strongly on the polarization of the incident light, we used a sheet polarizer, in conjunction with the white light source, to measure separately the efficiencies  $\epsilon_{\parallel}(\lambda)$  and  $\epsilon_{\perp}(\lambda)$  for light-polarized parallel and perpendicular to the grating grooves. We note that these curves are approximately the square (because there are two gratings) of the grating efficiency curves provided by the manufacturer, multiplied by the photomultiplier wavelength response function.

Because several detection schemes were used in the present work, we must be careful in our definitions of the coordinate axes. We define the primed set of axes ( $x'$ ,  $y'$ ,  $z'$ ) as the fixed coordinate axes of the heat pipe oven as shown in Fig. 1a. The vertical axis is labeled  $z'$  while the two lasers propagate along the  $x'$  axis. We also introduce an unprimed set of axes ( $x$ ,  $y$ ,  $z$ ) which are defined relative to the laser polarization and fluorescence detection directions. In this work, both lasers were linearly polarized along the same axis, which is taken to be  $z$ . Fluorescence was detected propagating in a direction lying in the  $xz$  plane at an angle  $\theta$  with respect to the  $z$  axis (see Fig. 1b). The OODR fluorescence was collected using three detection schemes.

*Scheme 1.* Both lasers are polarized vertically (i.e., the  $z$  axis coincides with the  $z'$  axis). Figure 2a gives a top view (along  $z'$ ) of the back fluorescence detection arrangement. A

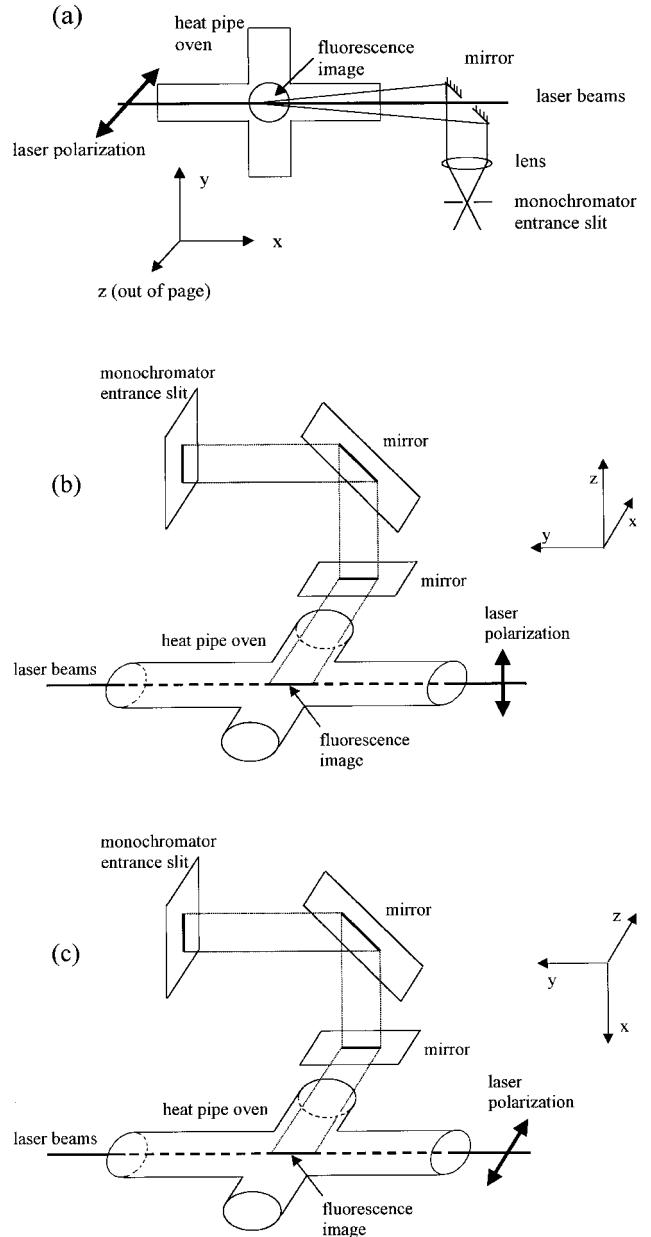


**FIG. 2.** (a) The back fluorescence collection scheme viewed from above along with the ( $x$ ,  $y$ ,  $z$ ) coordinate axes associated with this laser polarization and fluorescence detection scheme. Laser-induced fluorescence was collected through the entrance window of the PUMP and PROBE laser beams. (b) The arrangement for the side fluorescence collection scheme is shown along with the ( $x$ ,  $y$ ,  $z$ ) coordinate axes associated with this laser polarization and fluorescence detection scheme. Two mirrors were used to rotate the fluorescence image by  $90^\circ$ . Lenses were used to focus the fluorescence onto the slit but are not shown in the figure. (c) The top fluorescence collection scheme is shown along with the ( $x$ ,  $y$ ,  $z$ ) coordinate axes associated with this laser polarization and fluorescence detection scheme.

flat broadband high-reflection mirror with a 4-mm diameter hole in the middle is placed just outside one of the heatpipe windows along the laser propagation ( $x'$ ) axis. The surface of the mirror is oriented parallel to the  $z'$  ( $z$ ) axis and at a  $45^\circ$  angle relative to the  $x'$  and  $y'$  axes. The laser beams pass through the hole in the center of the mirror, but fluorescence emitted within a small solid angle propagating along the  $x'$  axis is reflected by the mirror and directed onto the entrance slit of the monochromator. Since the fluorescence detection direction is  $x'$ , the primed and unprimed coordinate systems coincide for this detection scheme, and the detection angle  $\theta = 90^\circ$ . In this arrangement, the  $z'$  direction of the oven interior (laser-polarization axis  $z$ ) is imaged parallel to the entrance slit and the grooves of the monochromator gratings. Similarly, the  $y'$  ( $y$ ) axis is imaged onto the slit but perpendicular to the slit and grating grooves. Since fluorescence light is collected from the entire laser path through the vapor, this scheme typically provides the largest fluorescence signals and is therefore of particular value for very weak signals. However, this scheme can suffer from contamination of the fluorescence signal with stimulated emission and/or laser scatter and care must be taken to avoid such problems. This fluorescence collection scheme is called *back* collection throughout this paper.

*Scheme 2.* Both lasers are polarized vertically. The lasers again propagate along the  $x'$  axis, but fluorescence is collected through a side window ( $y'$  direction) as shown in Fig. 2b. Thus the unprimed coordinate system is rotated  $90^\circ$  about the  $z'$  ( $z$ ) axis relative to the primed coordinate system ( $x = y'$  and  $y = -x'$ ). The detection angle  $\theta = 90^\circ$ . Two flat broadband mirrors are used to rotate the fluorescence image (which appears as a bright strip oriented along the laser propagation direction  $y = -x'$ ) from horizontal to vertical. In this arrangement, the  $x'$  axis of the oven interior ( $y$ ) is imaged onto the monochromator entrance slit, parallel to the slit, and parallel to the grooves of the gratings. The  $z'$  axis of the oven (laser-polarization axis  $z$ ) is imaged perpendicular to the slit and grating grooves. We note that this type of image rotation is commonly used in side direction fluorescence collection to maximize the light transmitted through the monochromator entrance slit. This scheme is called *side* collection throughout this paper.

*Scheme 3.* This scheme involves the same arrangement as scheme 2 except that we rotate the polarization directions of both lasers by  $90^\circ$  (i.e., both lasers are linearly polarized horizontally along the  $y'$  axis). In this arrangement, fluorescence is also collected from the side window, perpendicular to the laser propagation direction ( $x'$ ) but along the laser polarization direction (see Fig. 2c). Thus the unprimed coordinate system is obtained from the primed coordinate system by a  $-90^\circ$  rotation about the laser propagation ( $x'$ ) axis, followed by a  $90^\circ$  rotation about the new  $z$  axis (i.e.,  $x = -z'$ ,  $y = -x'$ , and  $z = y'$ ). The detection angle  $\theta = 0^\circ$ . Note that this detection scheme is equivalent to collecting fluorescence from

the top window if the laser polarizations had not been rotated. The image rotation mirrors again are used to rotate the fluorescence image from horizontal to vertical. Again, the  $x'$  axis of the oven interior ( $y$ ) is imaged onto the monochromator entrance slit, parallel to the slit, and parallel to the grooves of the gratings, while the  $z'$  axis ( $x$ ) is imaged perpendicular to the slit and grating grooves. However, since both  $x$  and  $y$  are perpendicular to the laser polarization direction, the image rotation has no effect in this case. This collection scheme is called *top* collection throughout this paper.

Figures 3a–3c display the resolved fluorescence spectra of the  $1^3\Sigma_g^- (v = 0, N = 9, J = 10) \rightarrow b^3\Pi_u (v' = 0)$  transitions with back, side, and top collection schemes, respectively. In Fig. 3b (side collection), the  $Q$  line is stronger than the  $P$  and  $R$  lines. However, in Fig. 3a (back collection), the relative intensities of the  $P$  and  $R$  lines remain the same, but the relative intensity of the  $Q$  line is weaker by a factor of 2. In Fig. 3c (top collection), the rotational pattern is similar to that displayed in Fig. 3b. Since the PUMP and PROBE lasers excite the same PFOODR transition for all three detection schemes, the differences of the relative intensities of the resolved fluorescence lines must be due to the differences between the three detection schemes.

A second example is given in Figs. 4a–4c, which show the resolved fluorescence spectra of the  $1^3\Delta_g (v = 17, N = 9, J = 10) \rightarrow b^3\Pi_u (v' = 4)$  transitions for the back, side, and top collection schemes, respectively. Here it can be seen that the relative intensities of the  $P$  and  $R$  lines remain the same, while the relative intensity of the  $Q$  line increases as we move from back to side to top collection. One final example is provided by Figs. 5a–5c, which display the resolved fluorescence spectra of the  $1^3\Delta_g (v = 9, N = 9, J = 10) \rightarrow b^3\Pi_u (v' = 9)$  transitions for the back, side, and top collection schemes, respectively. In Fig. 5b, the  $Q$  line is as strong as the  $R$  line and much stronger than the  $P$  line, but in Figs. 5a and 5c, the  $Q$  line is stronger than the  $R$  line by a factor of 2. In the next section, we analyze the emission and detection properties of the fluorescence in order to explain these results.

### Analysis

Due to the polarization of the excitation light field, laser-induced fluorescence invariably exhibits some degree of polarization and anisotropy. Molecular fluorescence lines corresponding to rotational transitions  $\Delta J = J_{\text{upper}} - J_{\text{lower}} = -1, 0,$  and  $+1$  ( $P$ ,  $Q$ , and  $R$  lines, respectively) have different polarization properties. Zare (4) has described the polarization behavior of fluorescence induced by a single linearly polarized light field. In the present work, the observed fluorescence was induced via two sequential transitions excited by two linearly polarized laser beams.

Figure 6 depicts the OODR excitation and resolved fluorescence energy level diagram for  $^7\text{Li}_2$ .  $|g\rangle$ ,  $|i\rangle$ ,  $|e\rangle$ , and  $|f\rangle$  are the ground ( $X^1\Sigma_g^+$ ), intermediate ( $b^3\Pi_u$ ), upper ( $1^3\Sigma_g^-$  or

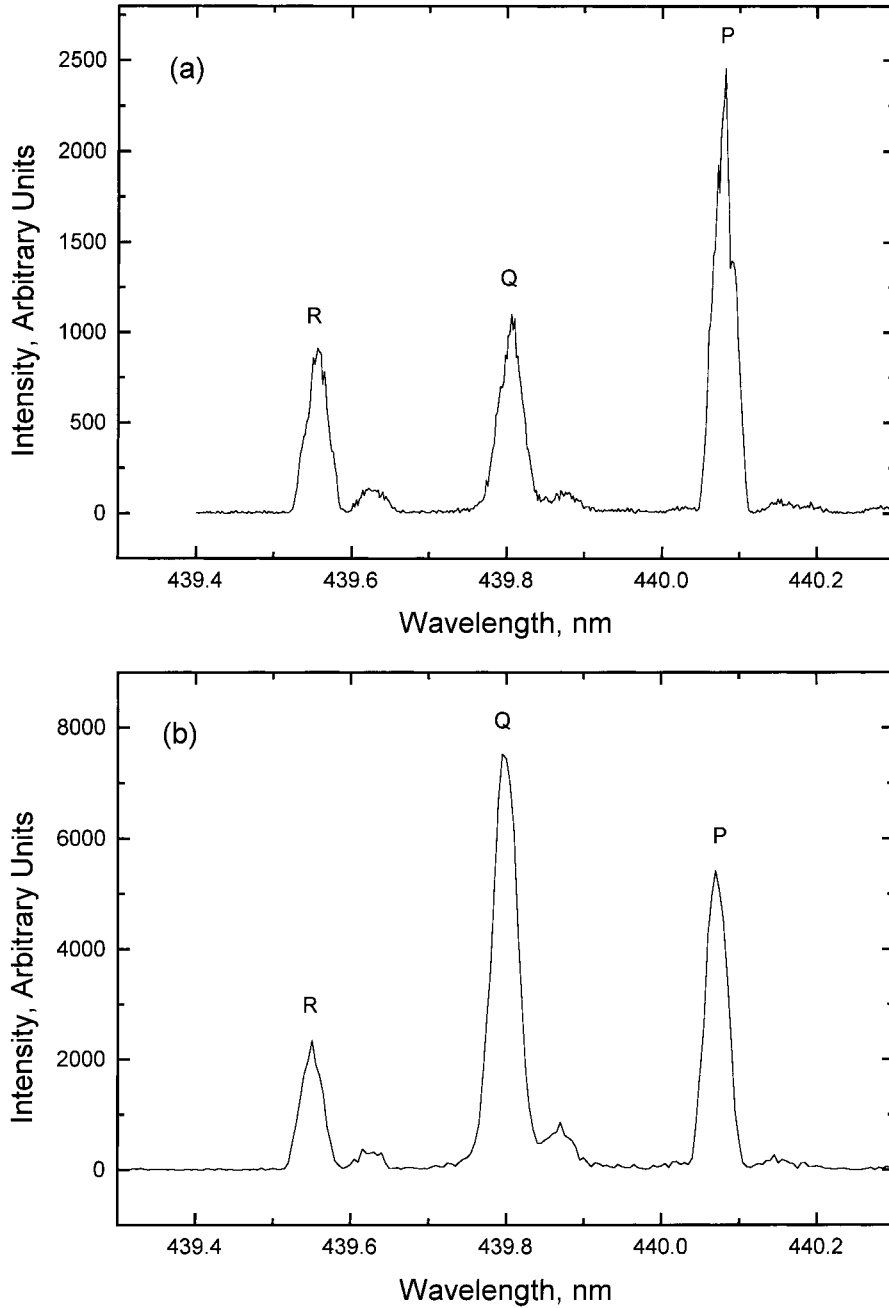


**FIG. 3.** Resolved fluorescence spectra of  $1^3\Sigma_g^-(v=0, N=9, J=10e) \rightarrow b^3\Pi_u(v'=0)$  transitions observed using (a) back, (b) side, and (c) top detection schemes.

$1^3\Delta_g$ ), and final ( $b^3\Pi_u$ ) levels, respectively.  $\hat{e}_1$ ,  $\hat{e}_2$ , and  $\hat{e}_3$  are the unit vectors (in general, complex) that specify the polarization of the electric field of the PUMP, PROBE, and fluorescence radiation, respectively. Let all states be characterized by good quantum numbers  $\alpha$ ,  $J$ , and  $M_J$ . Thus if we ignore the hyperfine structure, we may write  $|g\rangle = |\alpha_g, J_g, M_g\rangle$ ,  $|i\rangle = |\alpha_i, J_i, M_i\rangle$ ,  $|e\rangle = |\alpha_e, J_e, M_e\rangle$ , and  $|f\rangle = |\alpha_f, J_f, M_f\rangle$  (5). The ground state ( $|g\rangle$ ) is isotropic (i.e., all  $M_g$  levels are equally populated) in the absence of the PUMP laser.

The distribution of population within the intermediate state

$M_i$  sublevels,  $n_{J_i M_i}$ , pumped from the isotropic ground state by a weak (i.e., small intensity compared to the saturation intensity) linearly polarized laser is given by:

$$n_{J_i M_i} \propto \frac{n_{J_g}}{2J_g + 1} \sum_{M_g} |\langle \alpha_g J_g M_g | \hat{e}_1 \cdot \vec{\mu} | \alpha_i J_i M_i \rangle|^2, \quad [1]$$

where  $\vec{\mu} = e\vec{r}$  is the electric-dipole moment operator. The distribution of population within the upper state  $M_e$  sublevels,

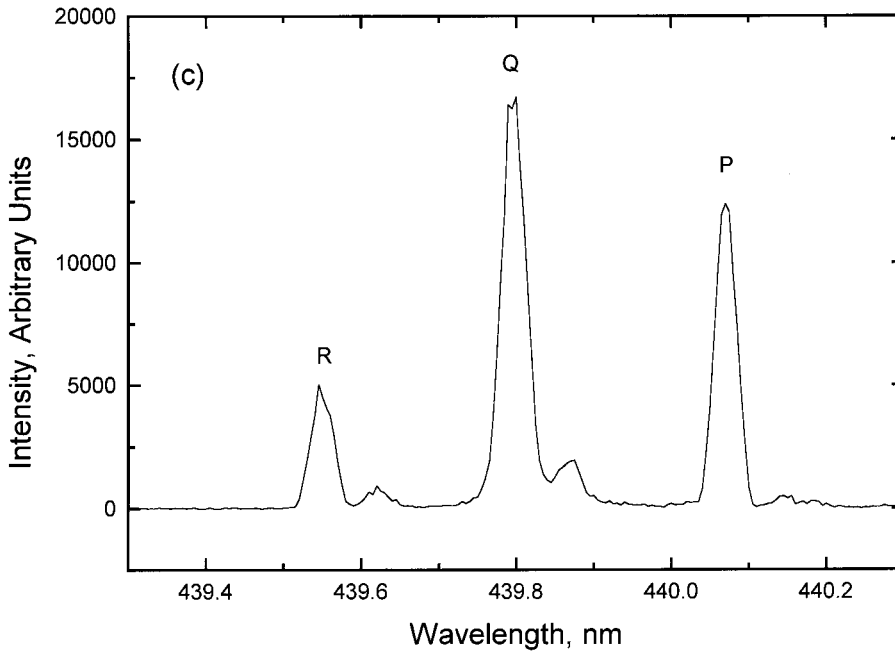


FIG. 3—Continued

$n_{J_e M_e}$ , pumped from the oriented or aligned intermediate state by a weak linearly polarized PROBE laser is given by:

$$n_{J_e M_e} \propto \sum_{M_i} n_{J_i M_i} |\langle \alpha_i J_i M_i | \hat{e}_2 \cdot \vec{\mu} | \alpha_e J_e M_e \rangle|^2. \quad [2]$$

The fluorescence from the anisotropically populated excited state to the final state is partially polarized. The intensity of fluorescence polarized along the  $\hat{e}_3$  direction is

$$I_{\hat{e}_3} \propto \sum_{M_f} \sum_{M_e} n_{J_e M_e} |\langle \alpha_e J_e M_e | \hat{e}_3 \cdot \vec{\mu} | \alpha_f J_f M_f \rangle|^2. \quad [3]$$

In the present work, both PUMP and PROBE lasers were polarized along the  $z$  axis, so that  $\hat{e}_1 = \hat{e}_2 = \hat{z}$  and  $\hat{e}_1 \cdot \vec{\mu} = \hat{e}_2 \cdot \vec{\mu} = \mu_z$ . [Note that the expressions given below would have to be modified if, for example, the lasers were circularly polarized or if the linear polarizations of the two beams were crossed.] The detection propagation direction lies in the  $xz$  plane at an angle  $\theta$ . We collect fluorescence with two orthogonal polarizations:  $I_{\perp}$  corresponding to polarization  $\hat{e}_3 = \hat{y}$ , which is orthogonal to the laser polarization axis, and  $I_{\parallel}$  corresponding to  $\hat{e}_3 = \sin \theta \hat{z} - \cos \theta \hat{x}$ , which is orthogonal to  $I_{\perp}$  but generally has a component along the laser polarization axis (see Fig. 1b). Thus we find

$$I_{\perp} \propto \frac{n_{J_g}}{2J_g + 1} \sum_{M_f} \sum_{M_e} \sum_{M_i} \sum_{M_g} |\langle \alpha_g J_g M_g | \mu_z | \alpha_i J_i M_i \rangle|^2 \times |\langle \alpha_i J_i M_i | \mu_z | \alpha_e J_e M_e \rangle|^2 |\langle \alpha_e J_e M_e | \mu_y | \alpha_f J_f M_f \rangle|^2 \quad [4]$$

and

$$I_{\parallel} \propto \frac{n_{J_g}}{2J_g + 1} \sum_{M_f} \sum_{M_e} \sum_{M_i} \sum_{M_g} |\langle \alpha_g J_g M_g | \mu_z | \alpha_i J_i M_i \rangle|^2 \times |\langle \alpha_i J_i M_i | \mu_z | \alpha_e J_e M_e \rangle|^2 \times |\langle \alpha_e J_e M_e | \mu_z \sin \theta - \mu_x \cos \theta | \alpha_f J_f M_f \rangle|^2. \quad [5]$$

The components of the dipole moment vector  $\vec{\mu}$  can be used to construct a spherical tensor operator  $\mu_q^k$  of rank  $k = 1$ :  $\mu_1^1 = -(2)^{-1/2} e(x + iy)$ ,  $\mu_0^1 = ez$ , and  $\mu_{-1}^1 = (2)^{-1/2} e(x - iy)$ . Then, according to the Wigner–Eckart theorem (4),

$$\langle \alpha J M | \mu_q^1 | \alpha' J' M' \rangle = (-1)^{1+J'-J} \langle J' M', 1q | JM \rangle \langle \alpha J || \vec{\mu} || \alpha' J' \rangle, \quad [6]$$

where  $\langle J' M', 1q | JM \rangle$  is the Clebsch–Gordan coefficient and  $\langle \alpha J || \vec{\mu} || \alpha' J' \rangle$  is the reduced matrix element. The square of the reduced matrix element is proportional to the linestrength (i.e., the Honl–London factor) of the  $J \rightarrow J'$  transition,

$$|\langle \alpha J || \vec{\mu} || \alpha' J' \rangle|^2 \propto S(J, J'), \quad [7]$$

which can be calculated from the formulas given by Kovacs (6), and the Clebsch–Gordan coefficient vanishes unless  $q + M' = M$ . Thus the quadruple sums in Eqs. [4] and [5] reduce to single sums over  $M_g \equiv M$  and the fluorescence intensities reduce to products of rotational linestrengths and Clebsch–Gordan coefficients:

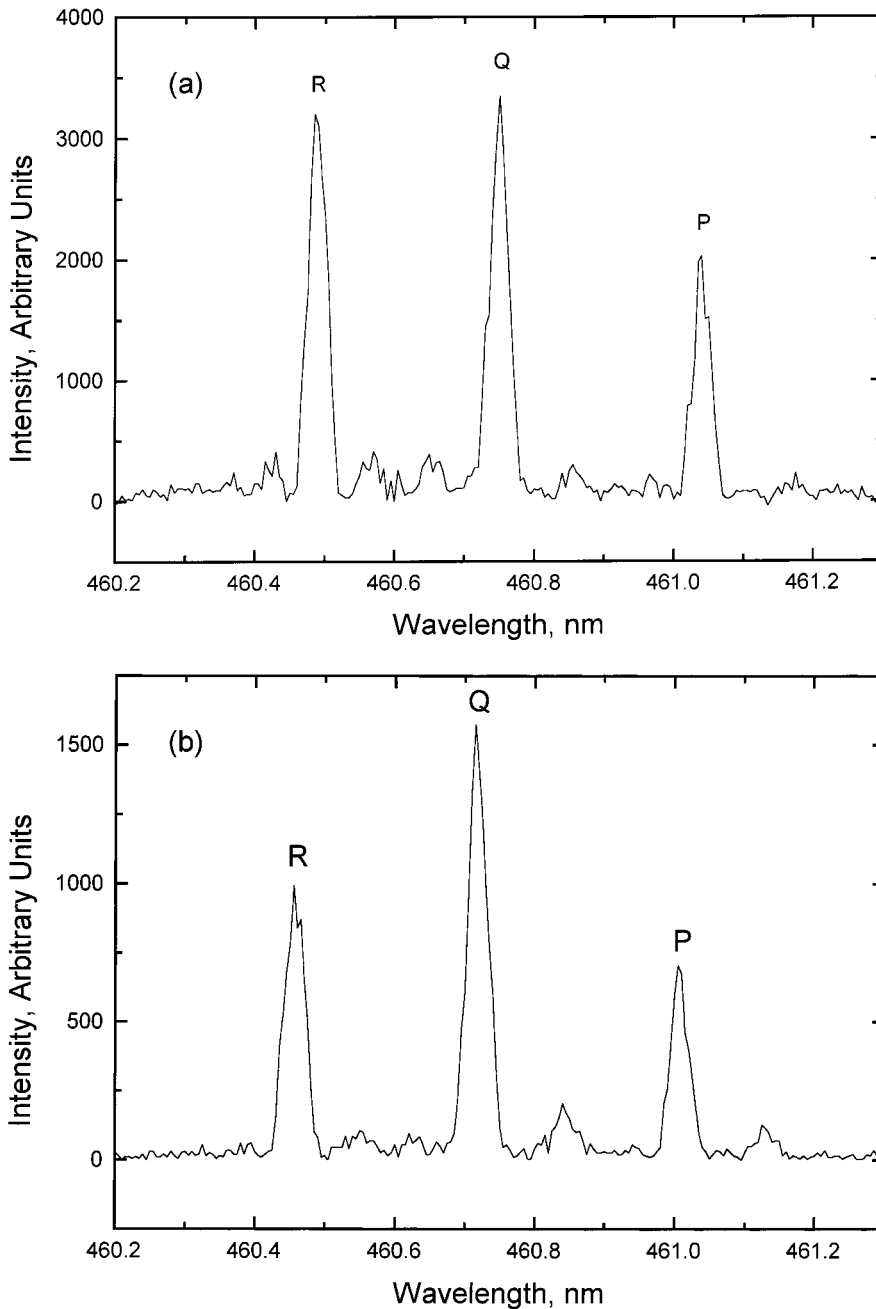


**FIG. 4.** Resolved fluorescence spectra of  $1^3\Delta_g$  ( $v = 17$ ,  $N = 9$ ,  $J = 10$ )  $\rightarrow$   $b^3\Pi_u$  ( $v' = 4$ ) transitions observed using (a) back, (b) side, and (c) top detection schemes.

$$\begin{aligned}
 I_{\perp} &\propto S(J_g, J_i)S(J_i, J_e)S(J_e, J_f) \frac{1}{2J_g + 1} \\
 &\times \sum_M \frac{1}{2} \{ |\langle J_f M - 1, 11 | J_e M \rangle|^2 \\
 &+ |\langle J_f M + 1, 1 - 1 | J_e M \rangle|^2 \} \\
 &\times |\langle J_e M, 10 | J_i M \rangle|^2 |\langle J_i M, 10 | J_g M \rangle|^2 \\
 &= S(J_g, J_i)S(J_i, J_e)S(J_e, J_f) A_{\perp}
 \end{aligned}$$

and

$$\begin{aligned}
 I_{\parallel} &\propto S(J_g, J_i)S(J_i, J_e)S(J_e, J_f) \frac{1}{2J_g + 1} \\
 &\times \sum_M \{ |\langle J_f M, 10 | J_e M \rangle|^2 \sin^2 \theta \\
 &+ \frac{1}{2} [ |\langle J_f M - 1, 11 | J_e M \rangle|^2
 \end{aligned}$$

[8]

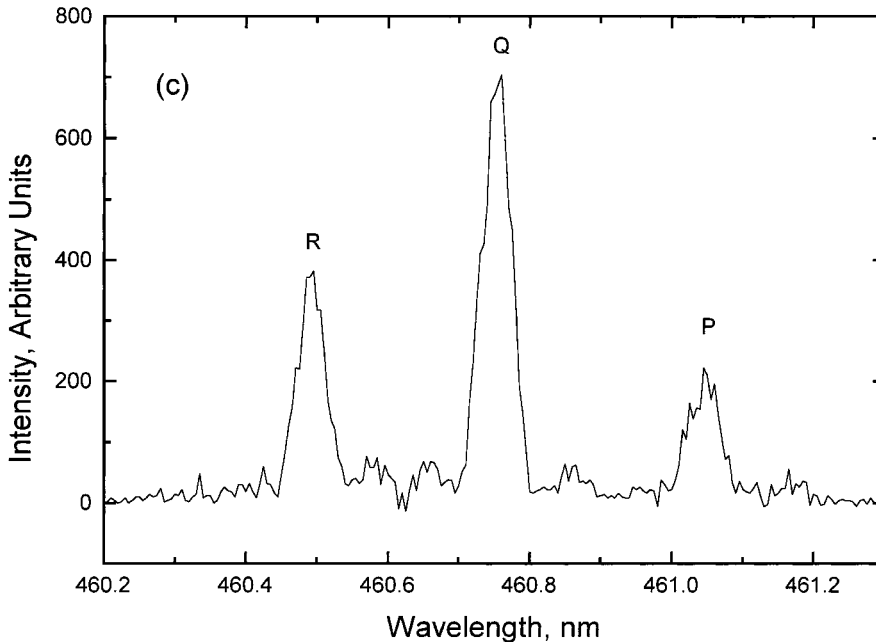


FIG. 4—Continued

$$\begin{aligned}
 & + |\langle J_f M + 1, 1 - 1 | J_e M \rangle|^2 \cos^2 \theta \} \\
 & \times |\langle J_e M, 10 | J_i M \rangle|^2 |\langle J_i M, 10 | J_g M \rangle|^2 \\
 = & S(J_g, J_i) S(J_i, J_e) S(J_e, J_f) [A_{\parallel} \sin^2 \theta + A_{\perp} \cos^2 \theta], \quad [9]
 \end{aligned}$$

with

$$\begin{aligned}
 A_{\perp} \equiv & \frac{1}{2J_g + 1} \sum_M \frac{1}{2} \{ |\langle J_f M - 1, 11 | J_e M \rangle|^2 \\
 & + |\langle J_f M + 1, 1 - 1 | J_e M \rangle|^2 \} \\
 & \times |\langle J_e M, 10 | J_i M \rangle|^2 |\langle J_i M, 10 | J_g M \rangle|^2
 \end{aligned} \quad [10]$$

and

$$\begin{aligned}
 A_{\parallel} \equiv & \frac{1}{2J_g + 1} \sum_M |\langle J_f M, 10 | J_e M \rangle|^2 \\
 & \times |\langle J_e M, 10 | J_i M \rangle|^2 |\langle J_i M, 10 | J_g M \rangle|^2.
 \end{aligned} \quad [11]$$

Note that the rotational line strength factors depend on the type of electronic transition considered, as well as the Hund's coupling case, but the factors  $A_{\perp}$  and  $A_{\parallel}$  only depend on the various  $J$  values as long as the hyperfine structure is not resolved in either the excitation or detection step. If the hyperfine structure is resolved, then  $A_{\perp}$  and  $A_{\parallel}$  are still given by Eqs. [10] and [11] (and  $I_{\perp}$  and  $I_{\parallel}$  by Eqs. [8] and [9]), but with the quantum numbers  $F$ ,  $M_F$  replacing  $J$ ,  $M_J$ . (If hyperfine structure is partially resolved, sums over contributing  $F$  as well as  $M_F$  values must be used in Eqs. [1]–[3] and carried through the subsequent analysis.)

It is important to emphasize that the intensities  $I_{\perp}$  and  $I_{\parallel}$

represent the two polarization components as they are emitted in the direction  $\theta$  from the center of the oven (see Fig. 1b). Thus these expressions do not yet take into account the effects of various mirrors (especially the image rotator used in schemes 2 and 3) that steer the fluorescence from the oven to the monochromator entrance slit.

The total fluorescence intensity radiated in the particular direction  $\theta$  (the sum of both polarizations) is given by

$$\begin{aligned}
 I_{\text{total}} = I_{\perp} + I_{\parallel} \propto & S(J_g, J_i) S(J_i, J_e) S(J_e, J_f) \\
 & \times [A_{\parallel} \sin^2 \theta + A_{\perp} (1 + \cos^2 \theta)]. \quad [12]
 \end{aligned}$$

Note that the total fluorescence emitted into all angles can be obtained from [12] by integrating over solid angle  $\sin \theta d\theta d\phi$ .

Finally, expressions for the detected signals are obtained by multiplying each polarization component by the wavelength-dependent detection system efficiency for that polarization at the appropriate wavelength. In this step, we must take into account the effects of the image rotator in schemes 2 and 3. We analyze each of the three detection schemes separately.

For scheme 1, back collection, we have  $\theta = 90^\circ$ ;  $I_{\parallel}$  is imaged along the grating grooves and  $I_{\perp}$  is imaged perpendicular to the grooves. The detected signal is thus

$$\begin{aligned}
 I_{\text{back}} = I_{\perp} \epsilon_{\perp} + I_{\parallel} \epsilon_{\parallel} & = \left[ \frac{A_{\perp} \epsilon_{\perp} + A_{\parallel} \epsilon_{\parallel}}{A_{\perp} + A_{\parallel}} \right] I_{\text{total}} \\
 & \propto S(J_g, J_i) S(J_i, J_e) S(J_e, J_f) [A_{\perp} \epsilon_{\perp} + A_{\parallel} \epsilon_{\parallel}]. \quad [13]
 \end{aligned}$$

For Scheme 2, side collection, we again have  $\theta = 90^\circ$ . There-

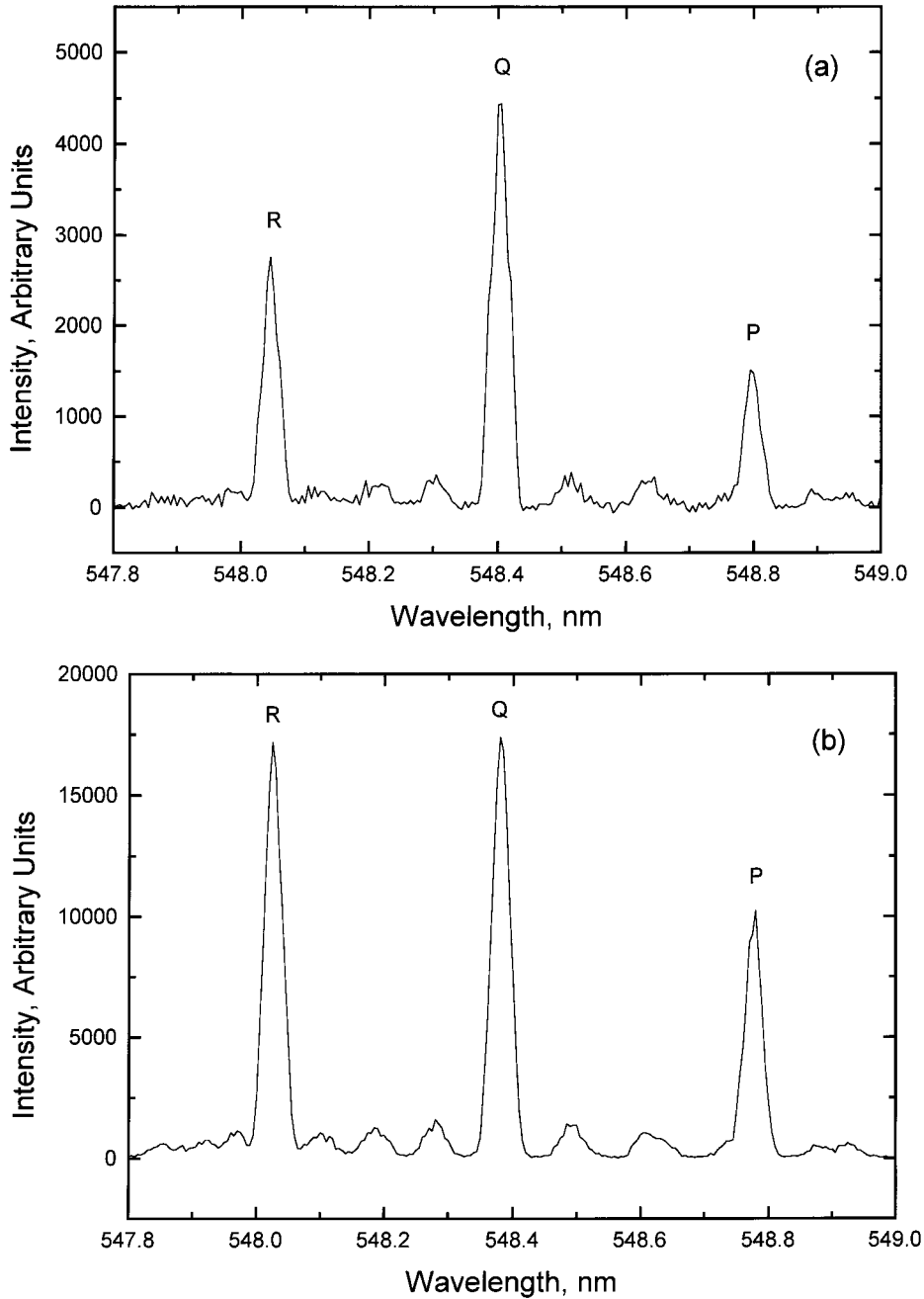


FIG. 5. Resolved fluorescence spectra of  $1^3\Delta_g(v=9, N=9, J=10) \rightarrow b^3\Pi_u(v=9)$  transitions observed using (a) back, (b) side, and (c) top detection schemes.

fore,  $I_{\perp}$  and  $I_{\parallel}$  are identical to those of scheme 1. But due to the image rotator,  $I_{\perp}$  is imaged along the grating grooves while  $I_{\parallel}$  is imaged perpendicular to the grooves. The detected signal is given by

$$I_{\text{side}} = I_{\perp}\epsilon_{\parallel} + I_{\parallel}\epsilon_{\perp} = \left[ \frac{A_{\perp}\epsilon_{\parallel} + A_{\parallel}\epsilon_{\perp}}{A_{\perp} + A_{\parallel}} \right] I_{\text{total}} \quad [14]$$

$$\propto S(J_g, J_i)S(J_i, J_e)S(J_e, J_f)[A_{\perp}\epsilon_{\parallel} + A_{\parallel}\epsilon_{\perp}].$$

Finally for scheme 3, top collection, we have  $\theta = 0^\circ$ , and

consequently  $I_{\perp}$  and  $I_{\parallel}$  are different from those of schemes 1 and 2. In the top collection case,  $I_{\perp}$  is imaged along the grating grooves and  $I_{\parallel}$  is imaged perpendicular to the grooves as in scheme 2. From Eqs. [8] and [9], we see that  $I_{\perp} = I_{\parallel} = I_{\text{total}}/2$  and the fluorescence emitted in this direction is unpolarized. The detected signal in this case is given by

$$I_{\text{top}} = I_{\perp}\epsilon_{\parallel} + I_{\parallel}\epsilon_{\perp} = \frac{1}{2}(\epsilon_{\parallel} + \epsilon_{\perp})I_{\text{total}} \quad [15]$$

$$\propto S(J_g, J_i)S(J_i, J_e)S(J_e, J_f)(\epsilon_{\parallel} + \epsilon_{\perp})A_{\perp}.$$

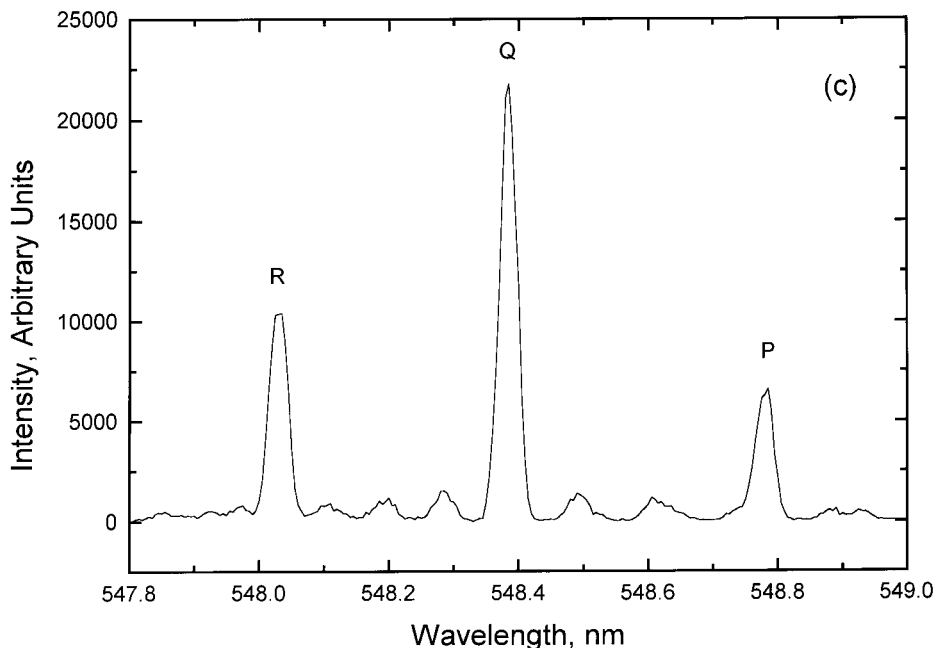


FIG. 5—Continued

The gratings of the Spex 1404 monochromator are holographic gratings with 1800 grooves/mm, whose reflectivity is strongly dependent on the polarization and the wavelength of the incident light (7). Figure 7a gives the polarization and wavelength dependence of the reflection efficiencies of a single grating, as provided by the manufacturer (8). We note that since the Spex 1404 is a double grating monochromator, the total efficiencies should be

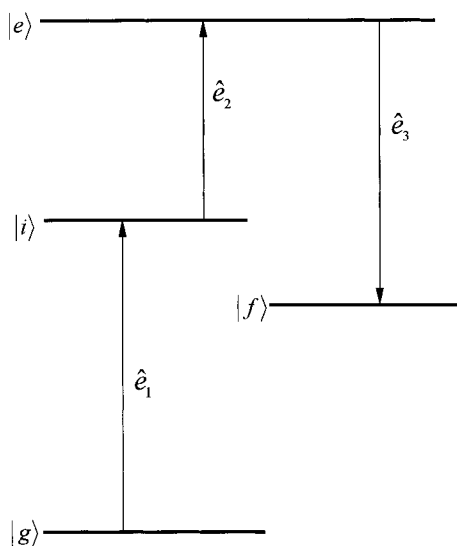


FIG. 6. Energy level diagram of the OODR excitation and resolved fluorescence spectra of  ${}^7\text{Li}_2$ .  $|g\rangle$ ,  $|i\rangle$ ,  $|e\rangle$ , and  $|f\rangle$  represent the ground ( $X^1\Sigma_g^+$ ), intermediate ( $b^3\Pi_u$ ), upper ( $1^3\Sigma_g^-$  or  $1^3\Delta_g$ ), and final ( $b^3\Pi_u$ ) levels, respectively.  $\hat{e}_1$ ,  $\hat{e}_2$ , and  $\hat{e}_3$  are unit vectors of the PUMP, PROBE, and fluorescence polarization, respectively.

given by the single grating curves squared. We also used a calibrated tungsten-halogen lamp (3) and a sheet polarizer to measure the total relative detection efficiencies, as a function of polarization and wavelength, for the complete detection system, including both gratings plus the photomultiplier tube (PMT). These results are given in Fig. 7b. The polarization dependence is determined almost entirely by the two gratings, while the overall wavelength dependence is determined by both the gratings and the PMT. Thus we expect that the measured ratio  $\epsilon_{\perp}(\lambda)/\epsilon_{\parallel}(\lambda)$  of Fig. 7b should agree with the square of the ratio of the single grating curves from Fig. 7a, and this appears to be roughly true. From Fig. 7 we can see that not only is the detection system efficiency wavelength dependent, but also strongly polarization dependent. The differences of the relative intensity patterns with back vs. side collection schemes, shown in Figs. 3 and 4, are *merely* a consequence of the different polarization efficiencies,  $\epsilon_{\perp}(\lambda)$  and  $\epsilon_{\parallel}(\lambda)$ , in combination with the image rotator used in the side collection scheme. On the other hand, the differences of the relative intensity patterns with side vs. top collection schemes, shown in Figs. 3, 4, and 5, result from the different polarization and angular distribution properties of the OODR  $P$ ,  $Q$ , and  $R$  fluorescence lines.

In Figs. 3, 4, and 5 the OODR excitation transitions are  $1^3\Sigma_g^- (v=0, N=9, J=10) \leftarrow b^3\Pi_u (v'=19, N'=10, J'=11) \leftarrow X^1\Sigma_g^+ (v''=4, J''=10)$ ,  $1^3\Delta_g (v=17, N=9, J=10) \leftarrow b^3\Pi_u (v'=19, N'=10, J'=11) \leftarrow X^1\Sigma_g^+ (v''=1, J''=10)$ , and  $1^3\Delta_g (v=9, N=9, J=10) \leftarrow b^3\Pi_u (v'=19, N'=10, J'=11) \leftarrow X^1\Sigma_g^+ (v''=1, J''=10)$ , respectively. Since the  ${}^7\text{Li}_2$   $b^3\Pi_u$  state is in the Hund's case b coupling limit,  $\Delta N \neq \Delta J$  transition strengths are much weaker than  $\Delta N = \Delta J$  transitions. In all three cases, the

**TABLE 1**  
**Ratios of Linestrengths  $S(J_\Lambda, J_\Pi)$  for  ${}^3\Lambda \rightarrow {}^3\Pi$  Transitions**

${}^3\Lambda \rightarrow {}^3\Pi$	<b>P : Q : R</b>		
	$J_{\text{upper}} = 10$	$J_{\text{upper}} = 30$	$J_{\text{upper}} = \infty$
F1 Components ( $N = J - 1$ )	1 : 2.578 : 1.713	1 : 2.175 : 1.186	1 : 2 : 1
F2 Components ( $N = J$ )	1 : 2.495 : 1.611	1 : 2.166 : 1.178	1 : 2 : 1
F3 Components ( $N = J + 1$ )	1 : 2.451 : 1.533	1 : 2.161 : 1.171	1 : 2 : 1
${}^3\Pi \rightarrow {}^3\Pi$	<b>P : Q : R</b>		
	$J_{\text{upper}} = 10$	$J_{\text{upper}} = 30$	$J_{\text{upper}} = \infty$
F1 Components ( $N = J - 1$ )	1 : 0.0213 : 0.9061	1 : 0.00226 : 0.9676	1 : 0 : 1
F2 Components ( $N = J$ )	1 : 0.0173 : 0.9059	1 : 0.00212 : 0.9676	1 : 0 : 1
F3 Components ( $N = J + 1$ )	1 : 0.0145 : 0.9071	1 : 0.00198 : 0.9676	1 : 0 : 1
${}^3\Sigma \rightarrow {}^3\Pi$	<b>P : Q : R</b>		
	$J_{\text{upper}} = 10$	$J_{\text{upper}} = 30$	$J_{\text{upper}} = \infty$
F1 Components ( $N = J - 1$ )	1 : 1.726 : 0.7339	1 : 1.903 : 0.9042	1 : 2 : 1
F2 Components ( $N = J$ )	1 : 1.733 : 0.7487	1 : 1.904 : 0.9062	1 : 2 : 1
F3 Components ( $N = J + 1$ )	1 : 1.755 : 0.7622	1 : 1.907 : 0.9081	1 : 2 : 1

Note that the  $S(J_\Lambda, J_\Pi)$  factors are calculated from the formulas of Tables 3.8 and 3.10 of Ref. 6. In the calculations, it is assumed that both the upper  ${}^3\Lambda$  and the lower  ${}^3\Pi$  states follow the Hund's case b coupling scheme, which is valid for all states of  $\text{Li}_2$ . Note also that line strengths for transitions with  $\Delta N \neq \Delta J$  are not listed in the table since, in the Hund's case b limit,  $\Delta N \neq \Delta J$  transitions are very weak except at very low  $J$ 's (less than ~1% for  $J \geq 10$ ) compared to the strongest ( $\Delta N = \Delta J$ ) transitions.

PUMP and PROBE transitions are  $\Delta J \equiv J_{\text{upper}} - J_{\text{lower}} = 1$  ( $R$ ) and  $-1$  ( $P$ ) transitions, respectively, and the three rotational lines in the  $1^3\Sigma_g^- \rightarrow b^3\Pi_u$  or  $1^3\Delta_g \rightarrow b^3\Pi_u$  fluorescence spectra correspond to  $\Delta J = -1, 0$ , and  $+1$  ( $P, Q$ , and  $R$  lines). For a given OODR excitation, the ratios of detected line intensities for back, side, and top detection schemes are obtained from Eqs. [13]–[15]:

$$\begin{aligned}
 \text{back:} \\
 I(P):I(Q):I(R) &= S(J_e, J_f = J_e + 1) \\
 &\times [A_\perp (J_f = J_e + 1)\epsilon_\perp (J_f = J_e + 1) \\
 &+ A_\parallel (J_f = J_e + 1)\epsilon_\parallel (J_f = J_e + 1)]: \\
 S(J_e, J_f = J_e) \\
 &\times [A_\perp (J_f = J_e)\epsilon_\perp (J_f = J_e) \\
 &+ A_\parallel (J_f = J_e)\epsilon_\parallel (J_f = J_e)]: \\
 S(J_e, J_f = J_e - 1) \\
 &\times [A_\perp (J_f = J_e - 1)\epsilon_\perp (J_f = J_e - 1) \\
 &+ A_\parallel (J_f = J_e - 1)\epsilon_\parallel (J_f = J_e - 1)],
 \end{aligned}$$

[16]

side:

$$\begin{aligned}
 I(P):I(Q):I(R) &= S(J_e, J_f = J_e + 1) \\
 &\times [A_\perp (J_f = J_e + 1)\epsilon_\parallel (J_f = J_e + 1) \\
 &+ A_\parallel (J_f = J_e + 1)\epsilon_\perp (J_f = J_e + 1)]: \\
 S(J_e, J_f = J_e) \\
 &\times [A_\perp (J_f = J_e)\epsilon_\parallel (J_f = J_e) \\
 &+ A_\parallel (J_f = J_e)\epsilon_\perp (J_f = J_e)]: \\
 S(J_e, J_f = J_e - 1) \\
 &\times [A_\perp (J_f = J_e - 1)\epsilon_\parallel (J_f = J_e - 1) \\
 &+ A_\parallel (J_f = J_e - 1)\epsilon_\perp (J_f = J_e - 1)],
 \end{aligned}$$

[17]

top:

$$\begin{aligned}
 I(P):I(Q):I(R) &= S(J_e, J_f = J_e + 1) \\
 &\times [\epsilon_\parallel (J_f = J_e + 1) + \epsilon_\perp (J_f = J_e + 1)] \\
 &\times A_\perp (J_f = J_e + 1):
 \end{aligned}$$

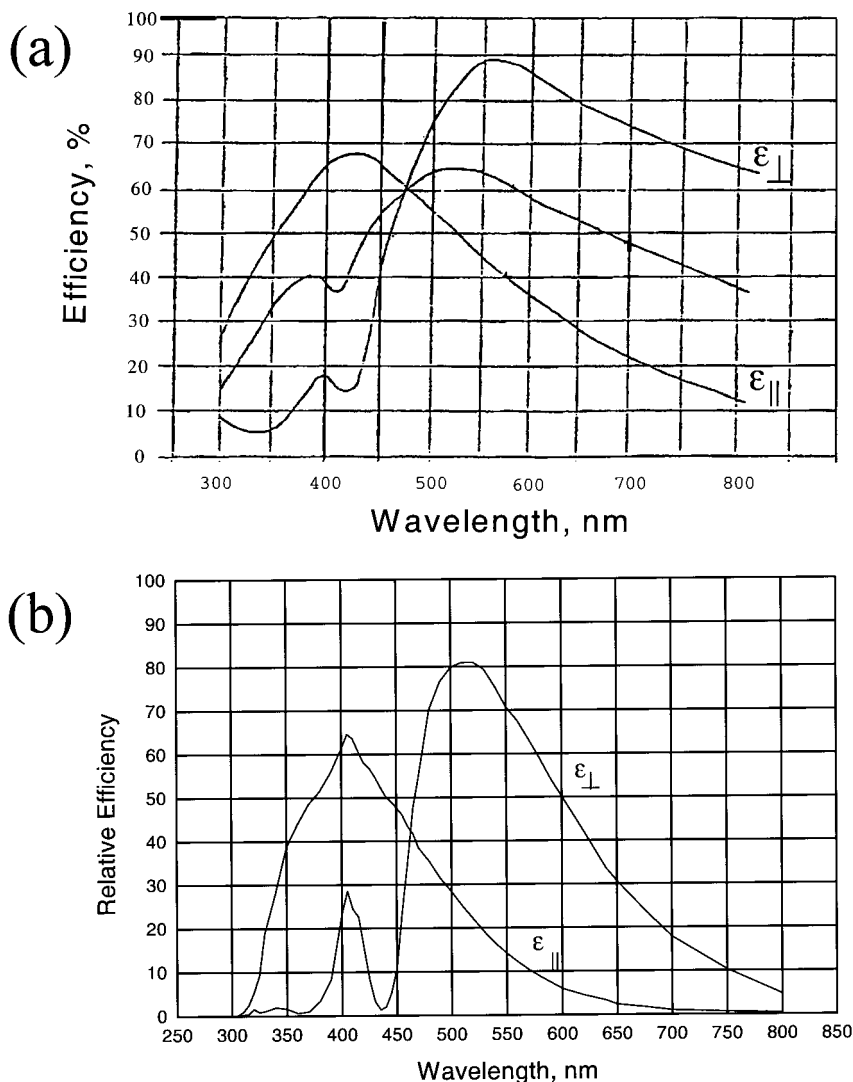


**FIG. 7.** (a) Reflection efficiency curves of a single holographic grating (1800 lines/mm) for the Spex 1404 monochromator.  $\epsilon_{\parallel}$  is the reflection efficiency for polarization direction parallel to the grooves ( $p$  plane), and  $\epsilon_{\perp}$  is the reflection efficiency for polarization perpendicular to the grooves ( $s$  plane). The middle curve is the reflection efficiency for unpolarized light  $\frac{1}{2}(\epsilon_{\perp} + \epsilon_{\parallel})$ . These curves were measured under Littrow conditions relative to the reflectance of aluminum (8). (b) Measured efficiency curves for the full detection system (both monochromator gratings and the PMT).

$$\begin{aligned}
 & S(J_e, J_f = J_e) \\
 & \times [\epsilon_{\parallel}(J_f = J_e) + \epsilon_{\perp}(J_f = J_e)] \\
 & \times A_{\perp}(J_f = J_e): \\
 & S(J_e, J_f = J_e - 1) \\
 & \times [\epsilon_{\parallel}(J_f = J_e - 1) + \epsilon_{\perp}(J_f = J_e - 1)] \\
 & \times A_{\perp}(J_f = J_e - 1). \quad [18]
 \end{aligned}$$

The Hund's case b relative line strengths  $S(J_e, J_f)$  of the  $P$ ,  $Q$ , and  $R$  fluorescence lines are listed in Table 1 for representative low and intermediate  $J_e = J_{\text{upper}}$  values (10 and 30, respectively) as well as for the  $J_e = J_{\text{upper}} = \infty$  limit (6). The  $A_{\perp}$  and  $A_{\parallel}$  values can be calculated from Eqs. [10] and [11] using, for

example, the formulas given on page 57 of Zare's book (4). These are listed in Table 2 for the same  $J_e$  values. Measured efficiencies,  $\epsilon_{\perp}(\lambda)$  and  $\epsilon_{\parallel}(\lambda)$ , at each relevant wavelength, are taken from Fig. 7b. With these data, we can use Eqs. [16]–[18] to calculate the ratios of  $P$ ,  $Q$ , and  $R$  fluorescence line intensities as observed using each detection scheme.

For the  ${}^7\text{Li}_2 1^3\Sigma_g^-$  case,  $J_g = 10$ ,  $J_i = 11$ ,  $J_e = 10$ . The calculated relative intensities of the  $P$ ,  $Q$ , and  $R$  lines after the monochromator with back, side, and top detection of  $1^3\Sigma_g^-$  ( $v = 0$ ,  $N = 9$ ,  $J = 10$ )  $\rightarrow b^3\Pi_u$  ( $v' = 0$ ,  $N' = 8, 9$ , and 10) emission are given in Table 3 where they are compared to the measured intensities for back vs. side vs. top detection schemes. We note that these fluorescence lines occur near  $\lambda = 440$  nm where  $\epsilon_{\perp}(\lambda)$  is very small (see Fig. 7b). Therefore, in

TABLE 2  
 $A_{\perp}$  and  $A_{\parallel}$  Values for  $P$ ,  $Q$ , and  $R$  Line Fluorescence Following Various OODR Excitation Schemes

Fluorescence transition	PUMP transition / PROBE transition	PP	PQ	PR	QP	QQ	QR	RP	RQ	RR	
P	$A_{\perp}$	$J_c = 10$	0.03968	0.02632	0.03680	0.02194	0.08279	0.02524	0.04130	0.02065	0.03810
		$J_c = 30$	0.03869	0.02472	0.03763	0.02318	0.08475	0.02429	0.03919	0.02272	0.03810
		$J_c = \infty$	0.03810	0.02381	0.03810	0.02381	0.08571	0.02381	0.03810	0.02381	0.03810
			(4/105)	(1/42)	(4/105)	(1/42)	(3/35)	(1/42)	(4/105)	(1/42)	(4/105)
	$A_{\parallel}$	$J_c = 10$	0.05398	0.02008	0.05370	0.01673	0.03381	0.02286	0.05738	0.01870	0.05714
		$J_c = 30$	0.05595	0.01938	0.05591	0.01816	0.03042	0.02032	0.05717	0.01901	0.05714
$J_c = \infty$		0.05714	0.01905	0.05714	0.01905	0.02857	0.01905	0.05714	0.01905	0.05714	
		(2/35)	(2/105)	(2/35)	(2/105)	(1/35)	(2/105)	(2/35)	(2/105)	(2/35)	
Q	$A_{\perp}$	$J_c = 10$	0.05541	0.01946	0.05539	0.01621	0.02892	0.02262	0.05899	0.01851	0.05905
		$J_c = 30$	0.05653	0.01920	0.05652	0.01800	0.02861	0.02019	0.05777	0.01888	0.05778
		$J_c = \infty$	0.05714	0.01905	0.05714	0.01905	0.02857	0.01905	0.05714	0.01905	0.05714
			(2/35)	(2/105)	(2/35)	(2/105)	(1/35)	(2/105)	(2/35)	(2/105)	(2/35)
	$A_{\parallel}$	$J_c = 10$	0.02251	0.03381	0.01653	0.02818	0.14156	0.02810	0.02199	0.02299	0.01524
		$J_c = 30$	0.02028	0.03042	0.01814	0.02852	0.14270	0.02852	0.02001	0.02668	0.01778
$J_c = \infty$		0.01905	0.02857	0.01905	0.02857	0.14286	0.02857	0.01905	0.02857	0.01905	
		(2/105)	(1/35)	(2/105)	(1/35)	(1/7)	(1/35)	(2/105)	(1/35)	(2/105)	
R	$A_{\perp}$	$J_c = 10$	0.03810	0.02701	0.03494	0.02251	0.08820	0.02550	0.03952	0.02086	0.03599
		$J_c = 30$	0.03810	0.02491	0.03700	0.02335	0.08662	0.02442	0.03857	0.02285	0.03744
		$J_c = \infty$	0.03810	0.02381	0.03810	0.02381	0.08571	0.02381	0.03810	0.02381	0.03810
			(4/105)	(1/42)	(4/105)	(1/42)	(3/35)	(1/42)	(4/105)	(1/42)	(4/105)
	$A_{\parallel}$	$J_c = 10$	0.05714	0.01870	0.05743	0.01558	0.02299	0.02233	0.06094	0.01827	0.06135
		$J_c = 30$	0.05714	0.01901	0.05717	0.01782	0.02668	0.02004	0.05841	0.01875	0.05846
$J_c = \infty$		0.05714	0.01905	0.05714	0.01905	0.02857	0.01905	0.05714	0.01905	0.05714	
		(2/35)	(2/105)	(2/35)	(2/105)	(1/35)	(2/105)	(2/35)	(2/105)	(2/35)	

Note. The PUMP transition/PROBE transition designation  $PQ$  means the PUMP laser excites a  $P$  line ( $J_{\text{upper}} = J_{\text{lower}} - 1$ ) while the PROBE excites a  $Q$  line ( $J_{\text{upper}} = J_{\text{lower}}$ ), etc. The PUMP and PROBE beam polarizations are parallel.  $J_c$  is the upper state rotational quantum number of the OODR excitation scheme (see Fig. 6). Numbers in parentheses refer to the  $J_c = \infty$  case.

this case, the monochromator is acting as an almost perfect polarizer. With  $\epsilon_{\perp}(\lambda) \approx 0$ , the back, side, and top detection scheme signals [see Eqs. [16]–[18]] reduce to  $I_{\text{back}} \propto A_{\parallel}\epsilon_{\parallel}$ ,  $I_{\text{side}} \propto A_{\perp}\epsilon_{\parallel}$ , and  $I_{\text{top}} \propto A_{\perp}\epsilon_{\parallel}$ . Since  $A_{\parallel}$  and  $A_{\perp}$  are very different

(especially for the  $Q$  line), we see a dramatic difference in the  $P:Q:R$  ratios for back and side detection. However, the side and top signals are virtually the same.

From our calculations we note that the ratio of  $R$  to  $P$  line

TABLE 3  
 Measured and Calculated OODR Fluorescence Line Intensity Ratios for  ${}^7\text{Li}_2$   $1^3\Sigma_g^-$  ( $v=0, N=9, J=10$ )  $\rightarrow$   $b^3\Pi_u$  ( $v=0$ ) Transitions Detected with the Back, Side, and Top Detection Schemes

	P : Q : R		
	back	side	top
measured	1 : 0.54 : 0.41	1 : 1.66 : 0.41	1 : 1.56 : 0.39
calculated	1 : 0.71 : 0.78	1 : 2.37 : 0.71	1 : 2.47 : 0.71

Note: the upper level was excited by the  $1^3\Sigma_g^-$  ( $v=0, N=9, J=10$ )  $\leftarrow$   $b^3\Pi_u$  ( $v'=19, N'=10, J'=11$ )  $\leftarrow$   $X^1\Sigma_g^+$  ( $v''=4, J''=10$ ) OODR transition. The fluorescence transitions occur near  $\lambda = 440$  nm.

TABLE 4

Measured and Calculated OODR Fluorescence Line Intensity Ratios for  ${}^7\text{Li}_2$   $1^3\Delta_g$  ( $\nu = 17, N = 9, J = 10$ )  $\rightarrow$   $b^3\Pi_u$  ( $\nu' = 4$ ) Transitions Detected with the Back, Side, and Top Collection Schemes

	P : Q : R		
	<i>back</i>	<i>side</i>	<i>top</i>
measured	1 : 1.83 : 1.73	1 : 2.45 : 1.54	1 : 2.98 : 1.55
calculated	1 : 1.99 : 1.73	1 : 2.21 : 1.71	1 : 3.66 : 1.62

Note: the upper level was excited by the  $1^3\Delta_g$  ( $\nu=17, N=9, J=10$ )  $\leftarrow$   $b^3\Pi_u$  ( $\nu'=19, N'=10, J'=11$ )  $\leftarrow$   $X^1\Sigma_g^+$  ( $\nu''=1, J''=10$ ) OODR transition. The fluorescence transitions occur near  $\lambda = 461$  nm.

intensities in the back, side, and top detection schemes should be approximately 0.7–0.8, while the observed ratio was, in fact, closer to 0.4 in both cases. This is due to a quantum interference effect: the upper  $1^3\Sigma_g^-$  ( $\nu = 0, N = 9, J = 10$ ) level is perturbed by the  $2^3\Pi_g$  ( $\nu = 26, N = 9, J = 10$ ) level ( $I$ ), and since both upper states have comparable transition amplitudes to the  $b^3\Pi_u$  ( $\nu' = 0$ ) level, quantum interference occurs (9). As a result of the perturbation, not only does the  $Q/(P + R)$  intensity ratio decrease, but also the  $P$  line becomes much stronger than the  $R$  line. Nonetheless, the differences between the back, side, and top detection scans are explained well by the ideas presented above.

Table 4 gives the calculated results for the  $1^3\Delta_g$  ( $\nu = 17, N = 9, J = 10$ )  $\rightarrow$   $b^3\Pi_u$  ( $\nu' = 4$ ) emission near  $\lambda = 461$  nm for back, side, and top detection and compares them to the measured ratios. In this case,  $\epsilon_{\perp}(\lambda)$  and  $\epsilon_{\parallel}(\lambda)$  are almost equal, which minimizes the polarizing effects of the monochromator. If  $\epsilon_{\perp}(\lambda)$  and  $\epsilon_{\parallel}(\lambda)$  were exactly equal, we would expect [from Eqs. [16]–[18]] that  $I_{\text{back}} \propto A_{\perp} + A_{\parallel}$ ,  $I_{\text{side}} \propto A_{\perp} + A_{\parallel}$ , and  $I_{\text{top}} \propto 2A_{\perp}$ . Thus the calculations indicate that the back and side rotational line intensity patterns should be similar. On the other hand, the  $Q$  line is enhanced in the top scan because  $A_{\perp}$  is much larger than  $A_{\parallel}$  for the  $Q$  line, while  $A_{\perp}$  is smaller than  $A_{\parallel}$  for the  $P$  and  $R$  lines. In general, the agreement between observation and calculation is very good in this case.

Table 5 gives the calculated results for the  $1^3\Delta_g$  ( $\nu = 9,$

$N = 9, J = 10$ )  $\rightarrow$   $b^3\Pi_u$  ( $\nu' = 9$ ) emission near  $\lambda = 548$  nm for back, side, and top detection and compares them to the measured ratios. In this case,  $\epsilon_{\perp}(\lambda)$  is much larger than  $\epsilon_{\parallel}(\lambda)$ . If we neglect the contributions to the signals from  $\epsilon_{\parallel}(\lambda)$ , we would expect [from Eqs. [16]–[18]] that  $I_{\text{back}} \propto A_{\perp}\epsilon_{\perp}$ ,  $I_{\text{side}} \propto A_{\parallel}\epsilon_{\perp}$ , and  $I_{\text{top}} \propto A_{\perp}\epsilon_{\perp}$ . Thus we expect that the back and top signals should be similar. However, we again have  $A_{\perp}$  much larger than  $A_{\parallel}$  for the  $Q$  line, while  $A_{\perp}$  is smaller than  $A_{\parallel}$  for the  $P$  and  $R$  lines. So we expect to see a dramatic drop of the  $Q$  line intensity relative to the  $P$  and  $R$  lines when we switch from top or back to side detection. Again, these ideas are confirmed by the detailed calculations and the measured intensity ratios.

The analysis given above is based on several assumptions whose validity must be considered. First, the  $M$  level populations given in Eqs. [1]–[3] are based on the weak field approximation. For these expressions to be valid, the PUMP and PROBE laser intensities must be small compared to the saturation intensities of the respective transitions. Second, we have ignored absorption and reemission of fluorescence photons (radiation trapping), which can revise the angular distribution of the fluorescence and scramble the polarization. Third, we have neglected the effects of collisions, which can mix the  $M$  level populations and thereby change the angular distribution and polarization properties of the fluorescence. Fourth, we have neglected the effects of magnetic fields in the vapor that

TABLE 5

Measured and Calculated OODR Fluorescence Line Intensity Ratios for  ${}^7\text{Li}_2$   $1^3\Delta_g$  ( $\nu = 9, N = 9, J = 10$ )  $\rightarrow$   $b^3\Pi_u$  ( $\nu' = 9$ ) Transitions Detected with the Back, Side, and Top Collection Schemes

	P : Q : R		
	<i>back</i>	<i>side</i>	<i>top</i>
measured	1 : 2.87 : 1.68	1 : 1.72 : 1.69	1 : 2.96 : 1.58
calculated	1 : 3.11 : 1.69	1 : 1.33 : 1.81	1 : 3.70 : 1.65

Note: the upper level was excited by the  $1^3\Delta_g$  ( $\nu=9, N=9, J=10$ )  $\leftarrow$   $b^3\Pi_u$  ( $\nu'=19, N'=10, J'=11$ )  $\leftarrow$   $X^1\Sigma_g^+$  ( $\nu''=1, J''=10$ ) OODR transition. The fluorescence transitions occur near  $\lambda = 548$  nm.

can also mix the  $M$  level populations and scramble the polarization. And finally, we must consider the fact that our narrow band lasers are able to partially resolve the hyperfine structure of the upper state, which has not been considered in the analysis presented above.

We have carried out some calculations and a series of experimental tests to estimate the importance of these effects under our experimental conditions. First, we note that because the intermediate level is a singlet–triplet mixture in all excitations described above, both PUMP and PROBE transitions may require higher laser power to be saturated. We studied the laser power dependence of the  $1^3\Delta_g$  ( $v = 9, N = 9, J = 10$ )  $\rightarrow$   $b^3\Pi_u$  ( $v' = 9$ ) fluorescence using the side detection scheme. In this case, we placed a polarizer in front of the monochromator entrance slit, oriented to transmit light polarized perpendicular to the grating grooves. This was done to enhance our sensitivity to the different polarizations and angular distributions of the  $P$ ,  $Q$ , and  $R$  lines. We found no significant change in the measured  $P:Q:R$  line intensity ratios as the PUMP (PROBE) power was lowered from 300 mW (270 mW) to 90 mW (110 mW) to 15 mW (20 mW). Thus we conclude that saturation effects are not dramatically altering the observed  $P:Q:R$  line intensity ratios presented here.

Second, we note that the lower levels of the observed fluorescence transitions are rovibrational levels of an excited electronic state ( $b^3\Pi_u$ ) which have negligibly small thermal populations. Thus it is unlikely for fluorescence photons to be reabsorbed in the vapor and we can safely neglect radiation trapping in the present experiment.

Third, we must consider the effects of  $M$  level changing collisions in  $\text{Li}_2$ . To the best of our knowledge, no measurements of cross sections for these collisions currently exist. However, experiments on depolarizing collisions of alkali atoms with noble gases have yielded cross sections of up to  $10^{-13}$   $\text{cm}^2$  (10, 11). At our experimental temperature ( $\sim 1000$  K) and buffer gas pressure ( $\sim 1$  Torr), we calculate  $M$  level mixing rates of  $\sim 5 \times 10^7$   $\text{s}^{-1}$  which is comparable to the radiative lifetimes of the excited molecules. Thus collisions must be considered to be a possible source of depolarization under our experimental conditions. However, we can test this effect by measuring fluorescence ratios as a function of pressure. Doing this using the  $1^3\Delta_g$  ( $v = 9, N = 9, J = 10$ )  $\rightarrow$   $b^3\Pi_u$  ( $v' = 9$ ) fluorescence (side detection scheme, polarizer in front of the monochromator entrance slit oriented to transmit light polarized perpendicular to the grating grooves), we find no significant changes in the fluorescence ratios (and hence in the polarizations) as the pressure was raised from 1.2 Torr to 3 Torr.

Next, we consider magnetic field effects on the polarization and angular distribution of the fluorescence lines. There are two sources of such magnetic fields. First, magnetic fields are produced by current-carrying wires used to heat the oven. This effect can be particularly important in cylindrical ovens where the heater wire is wound around the

cylinder in a solenoid configuration. However, in the present work, our heatpipe oven used “clam shell” heaters where the wires are oriented along the heatpipe axis, traveling up and back many times so that the heater-induced magnetic fields in the vapor tend to cancel. Moreover, the heaters were powered by ac supplies so that the directions of any such fields were reversed on a time scale that was fast compared to scans over individual fluorescence lines. A test for effects due to heater wire-induced magnetic fields was carried out by momentarily turning off the oven heaters while a scan was made (using the same transition and detection scheme as in the power and pressure dependence studies). The fluorescence pattern observed with the heater current off was identical to that observed with the current on. Second, we must worry about stray magnetic fields (such as the Earth’s field and those due to magnetic bases used for the optical mounts) that are present in the vapor. To be able to safely ignore the effects of such fields we require that the inverse of the Larmor precession frequency  $\omega_L^{-1} = \hbar/(g_J\mu_B B)$  be large compared to the lifetime of the excited state. Using a Gauss meter we measured magnetic fields of  $< \sim 1$  G near the center of the heatpipe oven. Thus we find  $\omega_L^{-1}$  is on the order of 100 ns which is indeed larger than the excited state lifetimes (12). Thus we expect some depolarization from stray fields, but not so much as to invalidate our conclusions.

Finally, we note that the hyperfine splittings of the  $b^3\Pi_u$  and  $1^3\Sigma_g^-$  states are sufficiently small that they can be safely neglected in the analysis. However, the  $1^3\Delta_g$  hyperfine structure is partially resolved under our experimental conditions (see also Ref. (13)). We carried out a test of the effects of partially resolved hyperfine structure on the  $P:Q:R$  line intensity ratios again using the  $1^3\Delta_g$  ( $v = 9, N = 9, J = 10$ )  $\rightarrow$   $b^3\Pi_u$  ( $v' = 9$ ) transitions and the same detection scheme as in the power, pressure, and heater current dependence studies. Here we kept the PUMP laser frequency fixed to line center of the  $b^3\Pi_u$  ( $v' = 19, N' = 10, J' = 11$ )  $\leftarrow$   $X^1\Sigma_g^+$  ( $v'' = 1, J'' = 10$ ) transition, while the frequency of the PROBE laser was varied within the  $1^3\Delta_g$  ( $v = 9, N = 9, J = 10$ )  $\leftarrow$   $b^3\Pi_u$  ( $v' = 19, N' = 10, J' = 11$ ) line profile. PROBE frequencies on the high- and low-frequency edges of the profile and near line center were used. Presumably a different combination of  $1^3\Delta_g$  ( $v = 9, N = 9, J = 10$ ) state hyperfine levels is pumped in each case. Again we found no significant differences between the  $P:Q:R$  fluorescence line intensity ratios measured using different PROBE frequencies. This seems to confirm that an analysis based on neglect of the hyperfine structure is valid.

We have also studied several other OODR excitations (14):

$$1^3\Sigma_g^- (v = 1, N = 21, J = 21f) \leftarrow$$

$$A^1\Sigma_u^+ (v' = 14, J' = 21) \leftarrow$$

$$X^1\Sigma_g^+ (v'' = 1, J'' = 22),$$

$$1^3\Sigma_g^-(v=1, N=33, J=32e) \leftarrow$$

$$A^1\Sigma_u^+(v'=15, J'=33) \leftarrow$$

$$X^1\Sigma_g^+(v''=2, J''=32),$$

$$1^3\Delta_g(v=9, N=10) \leftarrow$$

$$b^3\Pi_u(v'=19, N'=10, J'=11e) \leftarrow$$

$$X^1\Sigma_g^+(v''=1, J''=10),$$

and

$$1^3\Delta_g(v=17, N=10, 11) \leftarrow$$

$$b^3\Pi_u(v'=19, N'=10, J'=11e) \leftarrow$$

$$X^1\Sigma_g^+(v''=1, J''=10).$$

Using these and the previously described excitation transitions, we have measured and calculated relative intensities for resolved fluorescence lines of  $1^3\Sigma_g^-(v=1, N=21, J=21f) \rightarrow b^3\Pi_u(v'=0)$  and  $1^3\Sigma_g^-(v=1, N=33, J=32e) \rightarrow b^3\Pi_u(v'=0)$  emission with side and back detection,  $1^3\Delta_g(v=17, N=11) \rightarrow b^3\Pi_u(v'=4)$  emission with side and top detection, and  $1^3\Delta_g(v=9, N=9) \rightarrow b^3\Pi_u(v'=11)$ ,  $1^3\Delta_g(v=9, N=10) \rightarrow b^3\Pi_u(v'=9, 11)$ , and  $1^3\Delta_g(v=17, N=10) \rightarrow b^3\Pi_u(v'=4)$  emission with back, side, and top detection. Thus we have investigated  $RQ$ ,  $RR$ , and  $PQ$  PUMP/PROBE combinations in addition to the  $RP$  PUMP/PROBE scheme presented in Tables 3–5. Considering the uncertainty in measured fluorescence line intensities, as well as systematic errors associated with drift of the laser frequency or beam overlap during monochromator scans, the fact that hyperfine structure is ignored in the analysis and the depolarizing effects of collisions and magnetic fields, we believe the agreement of the observed and calculated relative intensities is satisfactory for all cases we have examined [except for the interference effect involving the  $1^3\Sigma_g^-(v=0, N=9, J=10)$  level discussed previously].

## CONCLUSIONS

Rotational branch intensity patterns in resolved fluorescence spectra are dependent on the choice of detection scheme. We analyzed the spectral patterns of  $^7\text{Li}_2$  PFOODR resolved fluorescence spectra dispersed by a Spex 1404 double grating monochromator with back, side, and top fluorescence detection

schemes. These pattern differences are due to the different polarization and anisotropic radiation patterns of  $P$ ,  $Q$ , and  $R$  fluorescence lines in OODR laser-induced fluorescence experiments, and the polarization and wavelength-dependent reflection efficiencies of the monochromator gratings.

## ACKNOWLEDGMENTS

We thank Prof. Frank Spano and Dr. Yaoming Liu for useful discussions, and Jianbing Qi for help with the experimental setup. This work was supported by NSF CHE-9320110 at Temple University and by NNSF (Grant 29773023) at Tsinghua University.

## REFERENCES

1. A. Yiannopoulou, B. Ji, Li Li, M. Li, K. Urbanski, A. M. Lyyra, W. C. Stwalley, and G.-H. Jeung, *J. Chem. Phys.* **101**, 3581–3587 (1994).
2. A. Yiannopoulou, K. Urbanski, A. M. Lyyra, Li Li, B. Ji, J. T. Bahns, and W. C. Stwalley, *J. Chem. Phys.* **102**, 3024–3031 (1995).
3. R. Stair, W. E. Schneider, and J. K. Jackson, *Appl. Opt.* **2**, 1151–1154 (1963).
4. Richard N. Zare, “Angular Momentum”, John Wiley & Sons, New York, 1988.
5. [The  $1^3\Delta_g$  state obeys the case  $b_{BS}$  hyperfine coupling scheme. Our calculations are based on the case  $b_{BJ}$  basis. These two bases are equivalent in the case where all hyperfine splittings are assumed to be unresolved in both excitation and detection stages.]
6. I. Kovacs, “Rotational Structure in the Spectra of Diatomic Molecules”, Hilger, London, 1969.
7. W. Demtröder, “Laser Spectroscopy”, Springer-Verlag, New York, 1982, p. 138.
8. [Information concerning the Spex Model 1404 double grating monochromator was provided by Instruments SA, Inc.]
9. H. Lefebvre-Brion and R. W. Field, “Perturbations in the Spectra of Diatomic Molecules”, Academic, Orlando, FL, 1986.
10. M. Lukaszewski and I. Jackowska, *Opt. Commun.* **46**, 89–92 (1983).
11. W. Kedzierski, R. B. Middleton, and L. Krause, *Phys. Rev. A* **43**, 143–146 (1991).
12. [Levels of the  $A^1\Sigma_u^+$  state have an average lifetime of 18.5 ns [W. Preuss and G. Baumgartner, *Z. Phys. A* **320**, 125–133 (1985)]. The  $b^3\Pi_u$   $F_1$  e-parity levels are metastable and can have very long radiative lifetimes. The  $A^1\Sigma_u^+(v=13, J=11) \sim b^3\Pi_u(v=19, N=10, J=11e)$  levels are strongly mixed. If the  $b^3\Pi_u$   $v=19, N=10$  level has 40% singlet character, it will have a lifetime of  $\sim 46$  ns. The  $1^3\Sigma_g^-$  state is a doubly excited valence state and its levels are expected to have lifetimes on the same order of magnitude as unperturbed  $A^1\Sigma_u^+$  state levels. No lifetime measurements currently exist for the  $1^3\Delta_g$  state. Since it is the lowest member of the  $nd^3\Delta_g$  Rydberg series and the  $3d-3p$  transition is a dipole-allowed transition, we expect the lifetime of the  $1^3\Delta_g$  state to be significantly shorter than 100 ns.]
13. Li Li, T. An, T.-J. Whang, A. M. Lyyra, W. C. Stwalley, R. W. Field, and R. A. Bernheim, *J. Chem. Phys.* **96**, 3342–3343 (1992).
14. The levels  $1^3\Sigma_g^-(v=1, N=21, J=21f)$  and  $1^3\Sigma_g^-(v=1, N=33, J=32e)$  are perturbed by the  $G^1\Pi_g(v=12, J=21f)$  and  $G^1\Pi_g(v=13, J=32e)$  levels, respectively. This makes them observable through  $A^1\Sigma_u^+$  intermediate levels.